PROCEEDINGS A

royalsocietypublishing.org/journal/rspa

Research

Cite this article: Dey S, Paul P, Ali SZ, Padhi E. 2020 Reynolds stress anisotropy in flow over two-dimensional rigid dunes. *Proc. R. Soc. A* **476**: 20200638.
http://dx.doi.org/10.1098/rspa.2020.0638

Received: 11 August 2020
Accepted: 29 September 2020

Subject Areas:
fluid mechanics

Keywords:
Reynolds stress anisotropy, turbulence anisotropy, Reynolds stress tensor

Authors for correspondence
Subhasish Dey
e-mail: sdey@iitkgp.ac.in
Prianka Paul
e-mail: mispaul05@iitkgp.ac.in
Sk Zeeshan Ali
e-mail: zeeshan@ce.iith.ac.in
Ellora Padhi
e-mail: ellora@iitkgp.ac.in

Reynolds stress anisotropy in flow over two-dimensional rigid dunes

Subhasish Dey[1], Prianka Paul[1], Sk Zeeshan Ali[2] and Ellora Padhi[1]

[1]Department of Civil Engineering, Indian Institute of Technology Kharagpur, West Bengal 721302, India
[2]Department of Civil Engineering, Indian Institute of Technology Hyderabad, Telangana 502285, India

SD, 0000-0001-9764-1346; PP, 0000-0002-6040-1784; SZA, 0000-0003-0763-7437; EP, 0000-0002-2295-2171

Characteristics of turbulence anisotropy in flow over two-dimensional rigid dunes are analysed. The Reynolds stress anisotropy is envisaged from the perspective of the stress ellipsoid shape. The spatial evolutions of the anisotropic invariant map (AIM), anisotropic invariant function, eigenvalues of the scaled Reynolds stress tensor and eccentricities of the stress ellipsoid are investigated at various streamwise distances along the vertical. The data plots reveal that the oblate spheroid axisymmetric turbulence appears near the top of the crest, whereas the prolate spheroid axisymmetric turbulence dominates near the free surface. At the dune trough, the axisymmetric contraction to the oblate spheroid diminishes, as the vertical distance below the crest increases. At the reattachment point and one-third of the stoss-side, the oblate spheroid axisymmetric turbulence formed below the crest appears to be more contracted, as the vertical distance increases. The AIMs suggest that the turbulence anisotropy up to edge of the boundary layer follows a looping pattern. As the streamwise distance increases, the turbulence anisotropy at the edge of the boundary layer approaches the plane-strain limit up to two-thirds of the stoss-side, intersecting the plane-strain limit at the top of the crest and thereafter moving towards the oblate spheroid axisymmetric turbulence.

THE ROYAL SOCIETY PUBLISHING

1. Introduction

Dunes that form in the sand and gravel of rivers, sea beaches, and deserts originate primarily due to the instability of the interface between the sediment bed and the driving fluid (both water and air) [1]. Research on the water or air flow over these bedforms would allow to precisely foresee the evolution of the planetary topography [2,3]. The diverse conditions of flow and sediment supply across the earth surface give rise to a wide variety of fluvial and aeolian dunes [1–8]. The mechanism that drives the dune formation is the characteristic phase lag between the sediment flux and the initial instabilities of the bedforms [1,3,9,10]. Particularly, in a fluvial environment of relatively coarse sediments of median size greater than 0.6 mm under a subcritical streamflow (i.e. flow velocity is less than the gravity wave celerity, but greater than the threshold velocity for the bed sediment motion), the sand and gravel dunes are formed [11]. They are scalene, triangular shaped, bearing a mildly sloping stoss-side (upstream slope) of about 6° and a steeply sloping leeside (downstream slope) roughly equalling the internal friction angle of sediments. They move streamwise by the action of flow having a free surface profile being out-of-phase with the wavy dune profile. It may however be noted that the field dunes in large rivers are mostly featured by complex leeside shapes and mild leeside slopes (less than 10°) [12]. Exploring the flow and turbulence characteristics in flow over subaqueous dunes, in particular, is of great interest to researchers [13,14], because their formation is closely linked with the underwater sediment transport and streambed stability. Dune hydrodynamics, which is a complex flow phenomenon, involves a separated flow emerging from the dune crest, followed by a recirculatory bubble within the valley formed by the neighbouring dunes being attached to the leeside of the preceding dune, a flow reattachment slightly in front of the trough, and a wake boundary layer over the stoss-side of the following dune [15]. Way back in 1914, more than a century ago, Gilbert [16] was the first to study the response of geophysical flows to dunes. Forty-four years later, Brooks [17] carried out more organized research to report that the response of flow to dunes becomes stronger with an increase in flow Froude number.

Among the promising experimental campaigns, Lyn [18] studied the turbulence quantities in flow over two-dimensional (i.e. spanwise symmetrical) rigid dunes to show that the near-bed turbulence quantities are influenced by the dune shape. McLean *et al.* [19] explored the turbulence structure in flow over a two-dimensional dune. They showed that the sediment transport over a dune is a nonlinear process, which is influenced by the statistics of velocity fluctuations in the flow zone close to the dune. Bennett & Best [20] reported that in flow over a two-dimensional dune, the maximum root-mean-square streamwise velocity fluctuations and the upward skewness of vertical velocity fluctuations occur along the shear layer of the separated flow. They argued that the strong ejection events are picked up from the Kelvin-Helmholtz (K-H) instabilities, which are the source of macro-turbulence structures. Kadota & Nezu [21] clarified the elemental structure of vortices using the flow visualization and measurements. They discussed the four-dimensional spatiotemporal structures of coherent vortices by evaluating the conventional correlation coefficients and the conditional statistics. They proposed a refined physics of coherent vortices. In order to distinguish the flow over two-dimensional and three-dimensional dunes, Maddux *et al.* [22] found that at a given vertical distance, the Reynolds shear stress over a two-dimensional dune is larger than that over a three-dimensional dune under an identical flow condition. However, the frictional resistance was reported to be higher in the latter case. The momentum flux in the flow over a three-dimensional dune was found to be driven by the secondary currents causing upward slower streamwise flow and downward faster streamwise flow. Venditti [23] experimentally detected the turbulence quantities and the drag over two-dimensional and three-dimensional dunes of different shapes. He concluded that these hydrodynamic quantities vary significantly with dune dimension and shape. Very recently, Dey *et al.* [15] performed an in-depth analysis of flow over two-dimensional dunes, shedding light on the flow kinematics, Reynolds stresses, dispersive stresses, higher-order correlations, turbulent kinetic energy (TKE) flux and budget, and bursting events, from the perspective of time- and

spatial averaging. They explained the mechanism of flow reattachment from the foundation of the Coandă effect. They argued that the decelerated flow zone downstream of the dune crest, encapsulating the occurrence of recirculation zone, gives rise to the kolk-boil vortex in the flow. In addition, they found the sweep and ejection events to govern the flow zones below and above the crest, respectively.

With regard to flow modelling, McLean & Smith [24] proposed a simple model for flow over two-dimensional dunes of a specific shape. Nelson & Smith [25] gave an improved flow model for velocity and boundary shear stress over two-dimensional dunes. The formation of a wake flow due to flow separation from the dune crest and its interaction with the inner boundary layer downstream of the flow reattachment point were treated using the method proposed by McLean & Smith [24]. Stoesser *et al.* [26] numerically simulated the turbulent flow field by using large eddy simulation (LES). However, their primary focus was on the coherent structures. They argued that the instantaneous separated vortices are formed downstream of the dune crest owing to the K-H instabilities. Close to the reattachment point, the so-called kolk-boil vortex develops in the form of a hairpin vortex. The separated vortices are convected along the stoss-side of the following dune moving towards the free surface. The near-bed fluid streaks that reorganize soon after the reattachment point were also prevalent in their study. Besides, the double-averaging methodology (DAM) was applied to synthesize the flow over dunes [15,27–31]. It was found that the implementation of the DAM has made the flow parametrization, modelling and phenomenological development rather convenient. The aforementioned research overview mainly focuses on the flow field and the flow modelling for the said problem without paying attention to the dune formation and the erodibility (sediment transport). These aspects are beyond the realm of the present study, because this study deals with the flow over two-dimensional rigid dunes.

It is worth highlighting that with regard to flow over dunes, the near-bed hydrodynamics was widely investigated by means of numerical simulations [26,32–38]. Due to the complex topography of dunes as often found in practical situations, resolving the near-bed flow and turbulence characteristics is highly challenging. Most frequently, the standard numerical models are unable to fully capture the essential elements of dune hydrodynamics due to the strong effects of flow separation and anisotropic character of near-bed turbulence. One of the prominent reasons of such failure is credited to the isotropic assumption on which the numerical models are founded. The above overview indicates that despite magnificent advances in understanding the hydrodynamics of flow over dunes, one of the key issues, *viz*., the characteristics of Reynolds stress anisotropy, remains unexplored for this kind of problem. The usefulness of analysing the turbulence anisotropy is that it effectively transforms the properties of a three-dimensional flow field to a two-dimensional plane formed by the invariant functions, reducing one degree of complexity [39]. Precise quantification of the turbulence anisotropy in flow over dunes offers a detailed picture of the relative contributions from the Reynolds stress tensor components, which have potential implications for the sediment transport and stability of bedforms [19,20]. For propagating mobile dunes, the sediment transport is largely driven by the spatio-temporally variable near-bed stress field. From a time-averaged sense, quantification of the spatial variation of the stress field over subaqueous dunes is important, because it is directly linked with the dune morphodynamics. Therefore, the knowledge of turbulence anisotropy is worthwhile for analysing the dune stability, which reflects a dynamic balance between the temporal evolution of the dune profile and the spatial gradient of sediment flux [38]. More broadly, high-fidelity experimental data of turbulence anisotropy in flow over dunes may shed new light on the validation and possible refinement of the traditional numerical models. The performance of numerical models largely depends on closure relationships, whose legitimacy can only be tested through novel experimental measurements. Hence, exploring the turbulence anisotropy over subaqueous dunes can offer guidance in enhancing the range of applicability of current numerical models. The turbulence anisotropy, which has so far been explored for various fluid mechanics problems, e.g. boundary layer flows, wall-wake flows and jet flows, is introduced below through a brief discussion.

From the perspective of turbulence foundation, an enriched insight into a fluid flow is essential to envisage the type of turbulence in regard to the degree of departure from the ideal isotropic turbulence, termed the *turbulence anisotropy*. The *Reynolds stress anisotropy tensor* is the most trustful entity to characterize the turbulence and to underpin the hypotheses, which are made in the classical theoretical development. In a turbulent flow, its second and third mathematical invariants together describe the possible states of realizable turbulence by means of the *anisotropic invariant map* (AIM) or the Lumley triangle [40–42]. It may be added that the anisotropy tensor invariants are integral to the Rotta model [43], describing the affinity of turbulence to return to an isotropic state at a rate linearly proportional to the degree of anisotropy in a turbulent flow. The current state of the art of research on the Reynolds stress anisotropy is primarily limited to the atmospheric boundary layer flows [44], flat-plate boundary layer flows [40,45–49], wall-wake flows [50–52], wake flows of wind turbine arrays [53–56], chemically reacting turbulent wall jet flows [57] and off-set jet flows [58]. It turns out that despite several decades of turbulence analysis, our knowledge of the Reynolds stress anisotropy in flow over dunes remains inadequate. The reason is ascribed to our current understanding of the turbulence anisotropy that is in fact incomplete, predominantly with respect to how the flow responds to the dunes.

Given the above appraisal, the objective of this study is to characterize the Reynolds stress anisotropy in flow over dunes. Additionally, in order to have an understanding of the overall flow structure over dunes, the physics of flow is briefly introduced here through the velocity vector and Reynolds shear stress plots before detailing the analysis of Reynolds stress anisotropy. To get a first-hand picture of the Reynolds stress anisotropy, the contours of the shape factor of stress ellipsoids formed by the Reynolds normal stresses are furnished on a non-dimensional spatial frame. In this study, the Reynolds stress anisotropy tensor is decomposed into its principle components related to a coordinate system. The second and third invariants of the scaled Reynolds stress tensor are plotted on the Lumley triangle in order to measure the state of turbulence in the dunal-bedform flow. In addition, the spatial evolutions of the anisotropic invariant function and the eigenvalues of the scaled Reynolds stress tensor are analysed in detail.

The novelty of this study comprises two key aspects. Firstly, it effectively advances the current state of the science of turbulence anisotropy in flow over subaqueous dunes. From the scientific rationale, this aspect sheds new light on the realization of stress ellipsoids formed by the Reynolds stresses. Secondly, it provides a discussion on the implications of the turbulence anisotropy from a modelling perspective. This aspect indicates the quest for new experimental data in calibrating and developing sophisticated numerical models. The organization of this paper is as follows. The experimentation is narrated in §2. The physics of flow over dunal bedforms is briefly described in §3, and the Reynolds stress anisotropy is critically analysed in §4. Lastly, the conclusion is drawn in §5.

2. Experimentation

An experiment was carried out to study the flow features over an artificially prepared bed with a series of two-dimensional dunes in a 15 m long flume of rectangular cross section (width × depth = $0.9 \times 0.75\,\mathrm{m}^2$) situated at the Hydraulics Laboratory, Indian Institute of Technology Kharagpur, India. Dunes that were created by uniformly graded gravels of median size $d = 9.75$ mm covering the entire flume length were rigidified by spraying an adhesive in order to prevent erosion by the flowing water. The gravel size was characteristically one to be often found in a natural riverbed with dunal bedforms [11]. Figure 1 shows the shape of the dunal bedforms, where each dune had a mild upstream slope forming the stoss-side of 0.425 m length (projected length on the streamwise axis) and a steep downstream slope forming the leeside (with a mild concave face) of 0.125 m length. The dune had a wavelength λ of 0.55 m and a height Δh of 0.04 m, maintaining the criterion $\lambda = 13.75\Delta h$, which is typically one that is frequently observed in a natural riverbed [11]. The dune bed had an average streamwise bed slope S_0 of 0.0004 (i.e. 1 in 2.5×10^3). This average bed slope was accrued by laying the series of identical dunes on the flume bottom from the same value of the flume bottom slope. The water flow flux in the flume

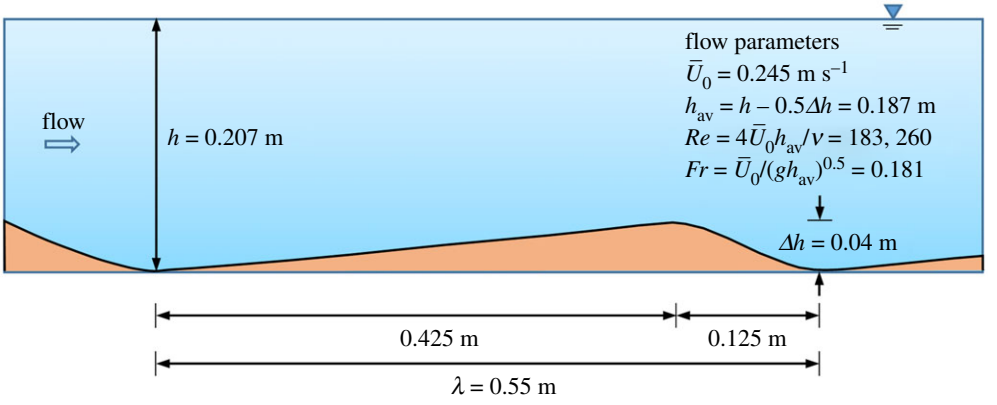

Figure 1. Sketch of the shape of a single dune in the experimentation. (Online version in colour.)

was measured by a calibrated V-notch weir and regulated by a valve, while the flow depth in the flume was adjusted by a downstream tailgate. The test section located at 8.25 m from the flume entrance was 1.65 m long (three wavelengths of dunes). The flow flux and the flow depth were regulated in such a way that the free-surface perturbation (undulation) within the test section measured by a Vernier point gauge was minimal (measured to be 2 mm). Note that the perturbed flow profile was essentially unavoidable owing to the bed undulations created by the dunes, but it was minimal. Therefore, the flow was deemed to have attained a quasi-uniform fully-developed free-surface flow. The maximum flow depth h (measured from the dune trough) was 0.207 m ($\pm 1 \times 10^{-3}$ m), (less than $6\Delta h$), satisfying the condition of scalene triangular dunes that are commonly observed in a natural riverbed [59]. Dey *et al*. [15] recognized that the dunal bedforms produce a macro-rough flow of *wake-interference flow* kind, in which the wake flow downstream of each dune intrudes the flow over the succeeding dune. It is, however, appropriate to estimate the average flow velocity $\bar{U}_0$ based on the average flow depth h_{av} ($= h - 0.5\Delta h$) [19,31]. We obtained the average flow velocity $\bar{U}_0 = 0.245\,\mathrm{m\,s^{-1}}$, the flow Reynolds number $Re(= 4\bar{U}_0 h_{av}/\nu) = 183\,260$ (confirming a turbulent flow), and the flow Froude number $Fr[= \bar{U}_0/(gh_{av})^{0.5}] = 0.181$ (confirming a subcritical flow), where ν is the coefficient of kinematic viscosity of fluid ($\approx 10^{-6}\,\mathrm{m^2\,s^{-1}}$) and g is the acceleration due to gravity.

The three-dimensional instantaneous velocity components in a Cartesian coordinate system were measured by a Nortek-manufactured down-looking acoustic Doppler velocimeter probe, named *Vectrino plus*. It was operated with an acoustic frequency of 10 MHz capturing the signals from a sampling location of 50 mm below the probe. Thus, the interference by the probe at the flow measuring location was minimal. The data acquisition was done at a sampling rate of 100 Hz for a duration of 240 s. The measurement was performed on the flume central plane over three wavelengths of dunes starting from the 16th dune. With reference to a Cartesian coordinate system (figure 2), x is the streamwise distance having the origin at 8.25 m from the flume entrance (i.e. the starting location of the 16th dune), and z is the vertical distance measured from the dune trough, whose origin lies between the 16th and the 17th dune. The resolutions of the flow measurements were 5 mm for $0 < z \leq 0.105$ m and 15 mm for $0.105\,\mathrm{m} < z \leq 0.155$ m, which could provide the complete flow structure satisfactorily [15]. In order to ascertain the errors associated with the flow measurements to be within the acceptable limit, uncertainty analysis was performed. To this end, the measurements were repeated three times and the samples were collected from several points in flow so as to keep away the reapplicability of the samples from bias and random errors. The results revealed that the errors were within 5% for the time-averaged velocity components and 8% for the Reynolds stresses. This confirmed the acceptability of the measured samples from the viewpoint of the uncertainty of measurements. Details of the experimental set-up and procedure, including the post processing (filtering, spike removal, etc.)

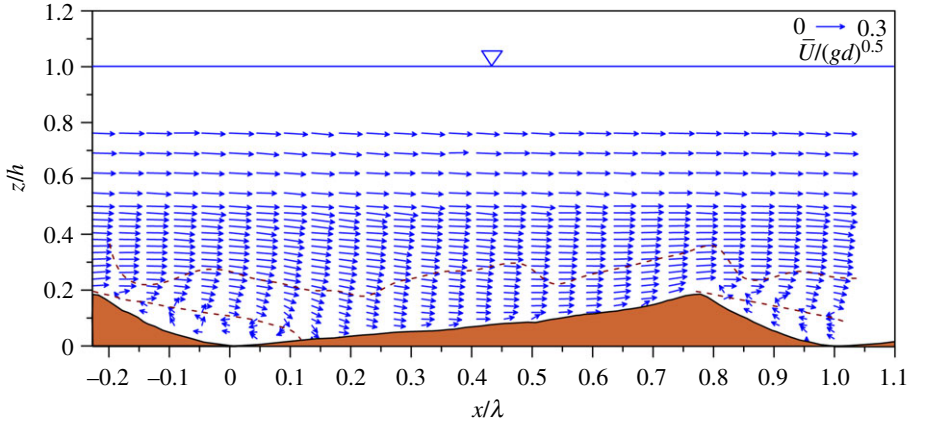

Figure 2. Non-dimensional time-averaged velocity vectors in flow over dunes on a vertical central plane. The lower broken line represents the flow separation line touching the bed at the reattachment point. The upper broken line, representing the locus of the inflection points of the $\bar{u}$ profiles, characterizes the extent of the inner boundary layer. (Online version in colour.)

of the raw samples collected by Vectrino system and their uncertainty analysis, are available in Dey *et al*. [15].

Dey *et al*. [15] investigated the important turbulence quantities in flow over a reach of three wavelengths of dunes (from the 16th to the 18th dune) from the perspective of their spatial averaging in addition to their time averaging over this reach. However, they paid no attention to analyse the Reynolds stress anisotropy. Therefore, it is interesting to shed light on this unexplored aspect of flow over dunes, because the state of the art of the Reynolds stress anisotropy is primarily limited to certain specified cases, as briefly stated in the introduction. As the objective of this study focuses on the Reynolds stress anisotropy rather than on the spatial averaging, we aim to probe the turbulence anisotropy over the 17th dune at specific key locations, *viz*., at trough, reattachment point, one- and two-thirds of stoss-side, crest and mid of leeside. The selection of these key sections is justified from the viewpoint of Dey *et al*. [15], who considered these sections in analysing the turbulence characteristics. It is however important to mention that the trends of the Reynolds stress anisotropy profiles at the identical sections over the 16th and the 18th dunes were almost similar to those over the 17th dune. This can be perceived from the principle of turbulence similarity.

3. Physics of flow over dunal bedforms

Although the primary focus of this study is to explore the Reynolds stress anisotropy in flow over dunes, a subtle glance at the behaviour of flow over dunes is worthwhile to understand the salient features of the physical system. In this context, it is worth mentioning that an in-depth description of flow physics over dunal bedforms has recently been reported elsewhere [15]. Despite this fact, the underlying physics of flow over dunal bedforms is summarized here to give the readers some key highlights of the dunal-bedform flow together with certain terminologies, which are used in §4. With regard to the physical system as sketched in figure 1, the non-dimensional time-averaged two-dimensional velocity vectors, having magnitude $\bar{U}/(gd)^{0.5}$ and direction arctan $(\bar{w}/\bar{u})$, in flow over dunes on a vertical central plane are illustrated in figure 2. Here, $\bar{U} = (\bar{u}^2 + \bar{w}^2)^{0.5}$, and $\bar{u}$ and $\bar{w}$ = time-averaged streamwise and vertical velocity components, respectively. It implies that the time-averaged two-dimensional velocity components $(\bar{u}, \bar{w})$ follow (x, z) directions. In figure 2, the velocity vector plots are shown on a non-dimensional spatial frame $(x/\lambda, z/h)$ over the stretch of a single dune (17th dune) with an additional leeside portion of the preceding dune. The origin $(x = 0, z = 0)$ of the axes is located at the trough that lies between the 16th and the 17th dunes.

Note that each dune can be thought to be a composite roughness element. As a result, the wall-shear flow experiences a regular variation of resistance provided by the macro-roughness formed by the series of dunes. It results in a flow heterogeneity, featuring a quasi-regular streamwise pattern, in the near-bed flow zone. This spatially recursive near-bed flow can be regarded as a wake-interference flow [15,60]. In this type of flow, the roughness elements are spanned so closely that the wake and vortex created from a roughness element intervene in those produced at the immediate downstream roughness element. It suggests a strong fluid mixing with an intricate vorticity field in the near-bed flow zone. In the present context, the inter-dune spacing is such that the wake generated from each dune crest interferes with the flow over the following dune (figure 2). It is pertinent to point out that the dune wavelength rather than the dune height plays an important role in creating the wake-interference flow. Furthermore, as the accelerated flow rushes over the stoss-side of the dunes ($x/\lambda = 0.12$–0.77), a near-bed layer of flow heterogeneity is apparent from figure 2 in the form of the dispersed velocity vectors originating from the local surface roughness over the dune surface. By contrast, a recirculation zone is formed on the leeside with a decelerated flow, which results from the separated flow downstream of the crest followed by a sudden expansion on the leeside. The recirculation region was evidently consistent on the leeside portions of both the neighbouring dunes (i.e. $x/\lambda = -0.227$–0.12 and 0.77–1.12). From figure 2, the no-slip condition at the dune bed is not obvious, because the closest measuring location from the bed was 2 mm above, where the near-bed velocity vectors are finite. A close observation reveals that the velocity declines rapidly, as one moves towards the bed, encapsulating that the no-slip is preserved at the bed.

The salient features of the flow structure over the dune encompass a separated shear layer from the dune crest with a recirculation zone on the leeside, a flow reattachment that spans up to $5\Delta h$ downstream of the crest, and an inner boundary layer (also called wake boundary layer) for the wake flow on the stoss-side of the dune. The recirculation zone is clearly recognized from the reversed flow at the immediate vicinity of the leeside. Note that in figure 2, the lower broken line demonstrates the flow separation line (locus of $\bar{u} = 0$) that touches the bed at the reattachment point, which is located just downstream of the trough. It suggests the location, where the accelerated fluid inrushes to the dune bed. The inner boundary layer is affected by the wake flow having an extremity along the locus (shown by the upper broken line in figure 2) of the inflection points of the $\bar{u}$ profiles. The inflection point up to which the effects of dunes are pronounced is defined as the point where the curvature of local time-averaged streamwise velocity vanishes ($\mathrm{d}^2\bar{u}/\mathrm{d}z^2 = 0$). However, above the flow reattachment, the wake flow layer involves a velocity defect. The inner boundary layer that prevails over the stoss-side of the following dune initiates from the reattachment point and it has a variable thickness (figure 2). This flow structure re-establishes over the following dunes one-after-another [15].

It is also interesting to explore the Reynolds shear stress in flow over dunes, because this is closely associated with the sediment transport and the bed stability for mobile dunes [19,20]. The Reynolds shear stress is expressed as $\tau_{uw} = -\rho\overline{u'w'}$, where ρ is the mass density of fluid and (u', w') are the fluctuations of instantaneous velocity components (u, w) with respect to their time-averaged values $(\bar{u}, \bar{w})$. Figure 3 shows the profiles of non-dimensional Reynolds shear stress $\tau_{uw}/(\rho g d)$ in flow over dunes on a vertical central plane. Over the dune stoss- and leeside, the τ_{uw} magnitudes increase, as the vertical distance z increases within the inner boundary layer (marked by the upper broken line in figure 3) attaining their individual peaks on the inner boundary layer. Thereafter, they dampen gradually, as one moves upwards. An intense fluid mixing resulting from the flow separation from the crest is the cause of occurrence of the peak in a given τ_{uw} profile. Note that the fluid mixing, on the other hand, dampens the fluid flux forming a wake flow downstream of the dune. The position of the peak of τ_{uw} rises downstream of the crest and then inclines downwards after the reattachment point. It is believed that the highly active kolk-boil vortex has an impact on the peak magnitude. However, the peak magnitudes in τ_{uw} profiles diminish along the stoss-side towards the crest due to the weakening of fluid mixing. Instead, inside the recirculation zone (whose extremity is shown by the broken line in figure 3) over the

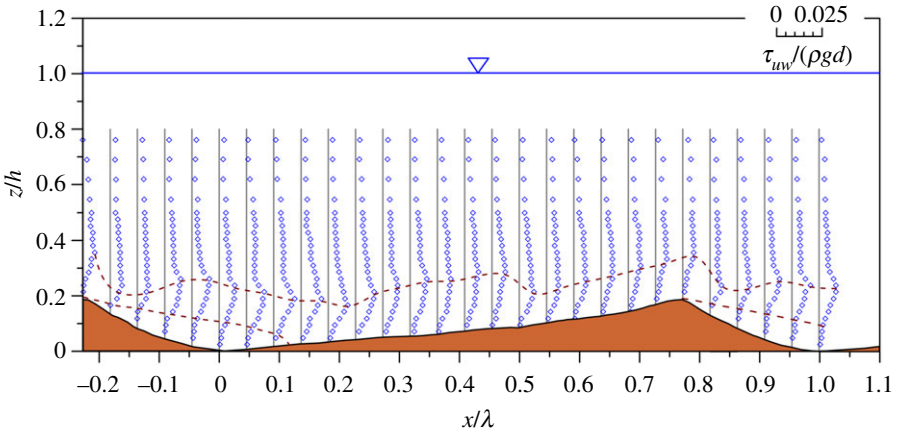

Figure 3. Profiles of non-dimensional Reynolds shear stress $\tau_{uw}/(\rho gd)$ in flow over dunes on a vertical central plane. The lower and upper broken lines represent the flow separation line and the extent of the inner boundary layer, respectively. (Online version in colour.)

leeside of the dune, the τ_{uw} diminishes. A repeatability in the Reynolds shear stress structure over the adjoining dunes was predominant.

The quantification of Reynolds shear stress serves as a guideline for obtaining the bed evolution for propagating mobile dunes. Note that an extrapolation of the τ_{uw} profile to the bed gives an estimate of the bed shear stress τ_0. When the bedload is the predominant mode of sediment transport, the equation of the sediment bed evolution follows: $(1-\rho_0)\partial\eta/\partial t + \partial q_b/\partial x = 0$, where ρ_0 is the porosity of sediment, $\eta(x,t)$ is the dune profile, t is the time and q_b is the bedload flux being a function of τ_0 [11]. With the precise formulation for the q_b, the $\eta(x,t)$ can be obtained by solving the above differential equation subject to suitable boundary conditions.

4. Reynolds stress anisotropy

Isotropic turbulence that is referred to as spherical turbulence corresponds to an idealized disorderly temporal fluid motion having no preferential direction. The foundation of isotropic turbulence belongs to the velocity fluctuations at a given point being independent of axis of reference or invariant with respect to axis rotation. It therefore indicates that the Reynolds normal stresses are identical, i.e. $\sigma_u = \sigma_v = \sigma_w$. Here, $(\sigma_u, \sigma_v, \sigma_w)$ are the Reynolds normal stresses in streamwise, spanwise and vertical directions, respectively, $[= \rho(\overline{u'u'}, \overline{v'v'}, \overline{w'w'})]$ and v' is the fluctuations of the instantaneous spanwise velocity component v with respect to its time-averaged value $\bar{v}$. On the other hand, in an anisotropic turbulence, the velocity fluctuations (u', v', w') are directionally biased making the Reynolds normal stresses no longer identical. It is therefore necessary to analyse the balance of Reynolds normal stresses from the outlook of the Reynolds stress anisotropy. The convenient way to produce a first-hand picture of turbulence anisotropy in the flow field over dunes is to plot the contours of shape factor S_σ of Reynolds stress ellipsoid, as shown in figure 4. The shape factor S_σ is expressed as $S_\sigma = \sigma_{\min}/(\sigma_{\max}\sigma_{\text{int}})^{0.5}$, where $\sigma_{\min}$, $\sigma_{\max}$ and σ_{int} are the minimum, maximum and intermediate values of Reynolds normal stress components at a point in a Cartesian coordinate system, respectively. Note that for an isotropic (i.e. spherical) turbulence, the S_σ becomes unity that corresponds to a Reynolds stress sphere, while for anisotropic turbulence, the S_σ is less than unity. In a natural turbulent flow field, such as in the present case, the turbulence is anisotropic, which is readily reflected from figure 4. It is evident that the anisotropy reduces within the valley formed by two neighbouring dunes, while it increases at the top of the crest. Overall, it appears that the Reynolds normal stresses are unequal $(\sigma_u \neq \sigma_v \neq \sigma_w)$, leaving a true signature of the anisotropic character of turbulence in flow over

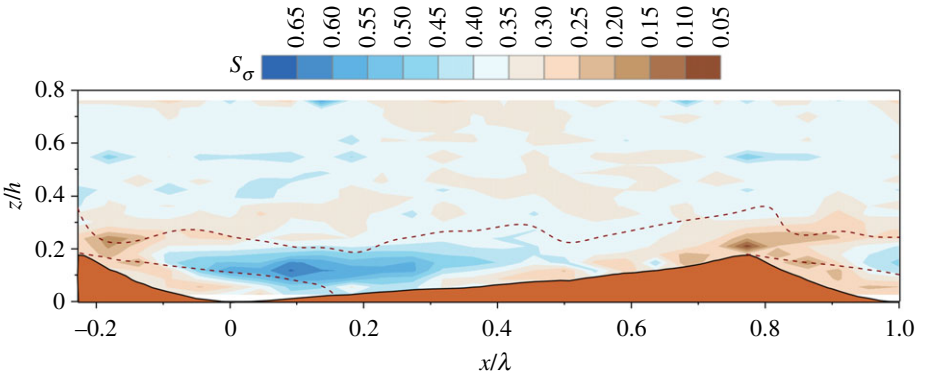

Figure 4. Contours of shape factor S_σ of Reynolds stress ellipsoid in flow over dunes on a vertical central plane. (Online version in colour.)

dunes. It is pertinent to mention that the effects of Reynolds normal stresses play a significant role in entraining sediment particles [61]. Even for a plane bed, the streamwise Reynolds normal stress can considerably affect the threshold bed shear stress for the streamwise motion of particles [62,63]. In addition, the vertical Reynolds normal stress is important for the particle uplift, because it is closely tied up with the vertical pressure gradient across the grain [64]. In exploring the turbulence characteristics over a two-dimensional dune, McLean *et al*. [19] also found substantial spatial growth of the combined probability distribution of the streamwise and vertical Reynolds normal stresses. Furthermore, it was evidenced that for a large bed shear stress exceeding the threshold bed shear stress, the combined effects of the bed shear stress (in the time-averaged sense) and the higher levels of turbulence can enhance the sediment entrainment rate significantly [65]. Reverting to the Reynolds stress anisotropy, a detailed analysis is given below.

Let us recall the Reynolds stress tensor $\overline{u_i' u_j'}$, which can be expressed as a positive semi-definite matrix. The required conditions for the positive semi-definiteness are as follows [66]:

$$\overline{u_\alpha' u_\alpha'} \geq 0, \quad \overline{u_\alpha' u_\alpha'} + \overline{u_\beta' u_\beta'} \geq 2\,|\,\overline{u_\alpha' u_\beta'}\,|, \quad \text{and} \quad \det(\overline{u_i' u_j'}) \geq 0, \quad \alpha, \beta = \{1, 2, 3\}. \tag{4.1}$$

The scaled Reynolds stress tensor, also termed the Reynolds stress anisotropy tensor b_{ij}, is expressed as

$$b_{ij} = \frac{\overline{u_i' u_j'}}{2k} - \frac{\delta_{ij}}{3}, \quad \delta_{ij} = \begin{cases} 1, & \text{if } i = j \\ 0, & \text{if } i \neq j \end{cases}, \tag{4.2}$$

where k is the TKE ($= \overline{u_i' u_i'}/2$). By definition, the b_{ij} is a symmetric and traceless tensor. To satisfy the semi-definiteness conditions given in equation (4.1), the characteristic ranges of diagonal and off-diagonal components of b_{ij} are expressed as

$$-\frac{1}{3} \leq b_{\alpha\alpha} \leq \frac{2}{3} \quad \text{and} \quad -\frac{1}{2} \leq b_{\alpha\beta} \leq \frac{1}{2}, \ \alpha \neq \beta. \tag{4.3}$$

For a second-order tensor with I_1, I_2 and I_3 being the principal invariants, the characteristic equation of b_{ij} is given by

$$\omega^3 - I_1 \omega^2 + I_2 \omega - I_3 I = 0, \tag{4.4}$$

where ω_{1-3} are the eigenvalues. According to the *Cayley-Hamilton theorem*, the b_{ij} satisfies its own characteristic equation. Therefore, equation (4.4) can also be expressed as

$$b_{ij}^3 - I_1 b_{ij}^2 + I_2 b_{ij} - I_3 \delta_{ij} = 0. \tag{4.5}$$

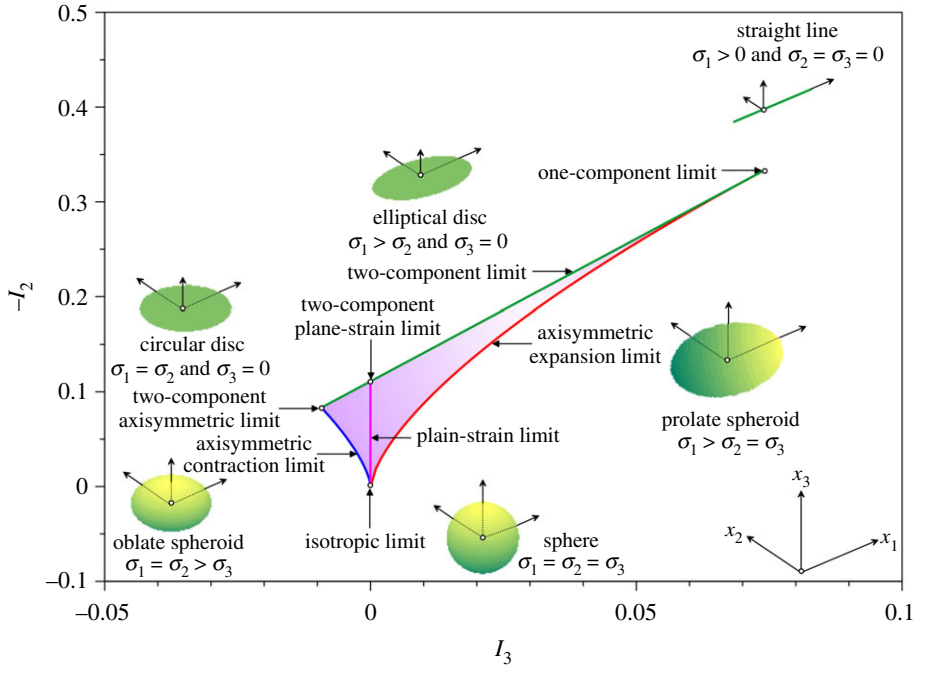

Figure 5. AIM on $-I_2I_3$ frame illustrating all possible realizations of turbulence states. (Online version in colour.)

As b_{ij} is a traceless tensor, by definition, $I_1 = 0$. The eigenvalues also satisfy $\omega_1 \geq \omega_2 \geq \omega_3$, $\omega_3 = -(\omega_1 + \omega_2)$, and the following conditions:

$$\omega_1(\omega_2 \geq 0) \geq \omega_2,\ \omega_1(\omega_2 < 0) \geq -2\omega_2, \quad \text{and} \quad \omega_1 + \omega_2 \leq \frac{1}{3}. \tag{4.6}$$

Importantly, equation (4.6) on I_2I_3 frame becomes

$$-I_2(I_3 \geq 0) \geq 3\left(\frac{I_3}{2}\right)^{2/3},\ -I_2(I_3 < 0) \geq -3\left(\frac{I_3}{2}\right)^{2/3} \quad \text{and} \quad -I_2 \leq 3I_3 + \frac{1}{9}. \tag{4.7}$$

Figure 5 shows the AIM, which is a conceptual representation of $-I_2$ versus I_3, obtained from equation (4.7). Equation (4.7) forms the Lumley triangle, having two curvilinear sides and one top-linear side on $-I_2I_3$ frame. Note that all the realizable states of turbulence are confined to the Lumley triangle on $-I_2I_3$ frame. The turbulence anisotropy has so far been envisioned from two different perspectives. The first perspective is based on the shape of turbulent eddies [67], whereas the other one being quite insightful is founded on the shape of the ellipsoid formed by the principal components of the Reynolds stresses [58,68].

From the perspective of the shape of turbulent eddies, the bottom, left and right vertices of the Lumley triangle correspond to *three-dimensional isotropic turbulence* ($-I_2 = I_3 = 0$), *two-component two-dimensional turbulence* and *one-component two-dimensional turbulence*, respectively. On the other hand, from the perspective of the shape of the ellipsoid formed by the principal components of the Reynolds stresses, the characteristics of the realizations of turbulence states are briefly given in table 1. The bottom vertex of the Lumley triangle corresponds to the *isotropic limit* (figure 5), where the stress ellipsoid appears to be a sphere ($\sigma_1 = \sigma_2 = \sigma_3$). Here, σ_{1-3} are the principal components of Reynolds stresses with respect to a set of coordinates (x_1, x_2, x_3). The left-curved side of the Lumley triangle corresponding to the *axisymmetric contraction limit* makes the stress ellipsoid an *oblate spheroid*, because one principal component is smaller than the other two equal components ($\sigma_1 = \sigma_2 > \sigma_3$). However, at the left vertex that refers to a *two-component axisymmetric limit*, the stress ellipsoid becomes a *circular disc* owing to two equal principal components

Table 1. Characteristics of the realizations of turbulence states.

turbulence state	invariants	shape of principal components of Reynolds stresses
isotropic	$-I_2 = I_3 = 0$	sphere
axisymmetric contraction limit	$-I_2 = -3(I_3/2)^{2/3}$	oblate spheroid
two-component axisymmetric limit	$-I_2 = 1/12, I_3 = -1/108$	circular disc
axisymmetric expansion limit	$-I_2 = 3(I_3/2)^{2/3}$	prolate spheroid
two-component limit	$-I_2 = 3I_3 + 1/9$	elliptical disc
one-component limit	$-I_2 = 1/3, I_3 = 2/27$	straight line

with a vanishing third component ($\sigma_1 = \sigma_2$ and $\sigma_3 = 0$). The right-curved side of the Lumley triangle corresponding to the *axisymmetric expansion limit* represents a *prolate spheroid*, because one principal component is larger than the other two equal components ($\sigma_1 > \sigma_2 = \sigma_3$). Note that both axisymmetric contraction and expansion limits are symmetric about the line $I_3 = 0$, termed the *plane-strain limit* (figure 5). Furthermore, on the top-linear side of the Lumley triangle representing the *two-component limit*, the stress ellipsoid forms an *elliptical disc*. The reason is that one principal component is larger than the other one together with a third component that disappears ($\sigma_1 > \sigma_2$ and $\sigma_3 = 0$). The plane-strain limit intersects the two-component limit at a point, termed the *two-component plane-strain limit*. Moreover, the right vertex of the Lumley triangle signifies the *one-component limit*, where the stress ellipsoid appears to be a *straight line* owing to one finite component along with two other vanishing components ($\sigma_1 > 0$, $\sigma_2 = \sigma_3 = 0$).

To find how the turbulence anisotropy evolves with the streamwise distance, we consider various characteristic sections over the dunes as shown at the top of figure 6. Figure 6*a–f* depicts the AIMs at various non-dimensional streamwise distances, x/λ = 0 (trough), 0.23 (reattachment point), 0.257 (one-third of stoss-side), 0.515 (two-thirds of stoss-side), 0.772 (crest) and 0.886 (mid of leeside), respectively. Note that in figure 6*a–f*, the top-linear side of the Lumley triangle is not shown, because the experimental data points are almost confined to the flank of the right- and left-curved sides of the Lumley triangle. Different symbols (diamonds, squares and circles) are used to distinguish the data points in three different flow layers, such as below crest, crest to edge of boundary layer and outer flow layer, respectively. Here, the edge of the boundary layer with regard to a given streamwise distance refers to the inflection point, where $\mathrm{d}^2\bar{u}/\mathrm{d}z^2 = 0$. In addition, the experimental data points corresponding to the crest and the edge of the boundary layer are highlighted (see filled diamonds and filled squares). At a given streamwise distance, the evolution of turbulence anisotropy with an increase in vertical distance is shown by a broken line with an arrowhead. At the dune trough (figure 6*a*), the data plots in the immediate near-bed flow zone stay close to the left-curved side of the Lumley triangle. However, as the vertical distance increases, the data plots suggest that the turbulence anisotropy appears to return to the isotropic limit following a path almost parallel to the axisymmetric contraction limit. This reveals that as the vertical distance increases, the turbulence anisotropy diminishes tending to the three-dimensional isotropy. As the vertical distance increases further, the data plots appear to take a swift clockwise turn in the direction of the left-curved side of the Lumley triangle, suggesting a changeover of the turbulence anisotropy from the quasi-three-dimensional isotropic state to the axisymmetric contraction limit. The AIM indicates that at the top of the crest, the turbulence anisotropy closely follows the axisymmetric contraction limit. Beyond the crest, the data plots take a rightward turn with an increase in vertical distance, crossing the plane-strain limit and thereafter tend to move towards the right-curved side of the Lumley triangle (figure 6*a*). This indicates that the turbulence anisotropy switches from the axisymmetric contraction limit to the axisymmetric expansion limit, as the vertical distance increases, in particular within the outer flow layer. It is notable that the data plots up to the edge of the boundary layer appear to form a

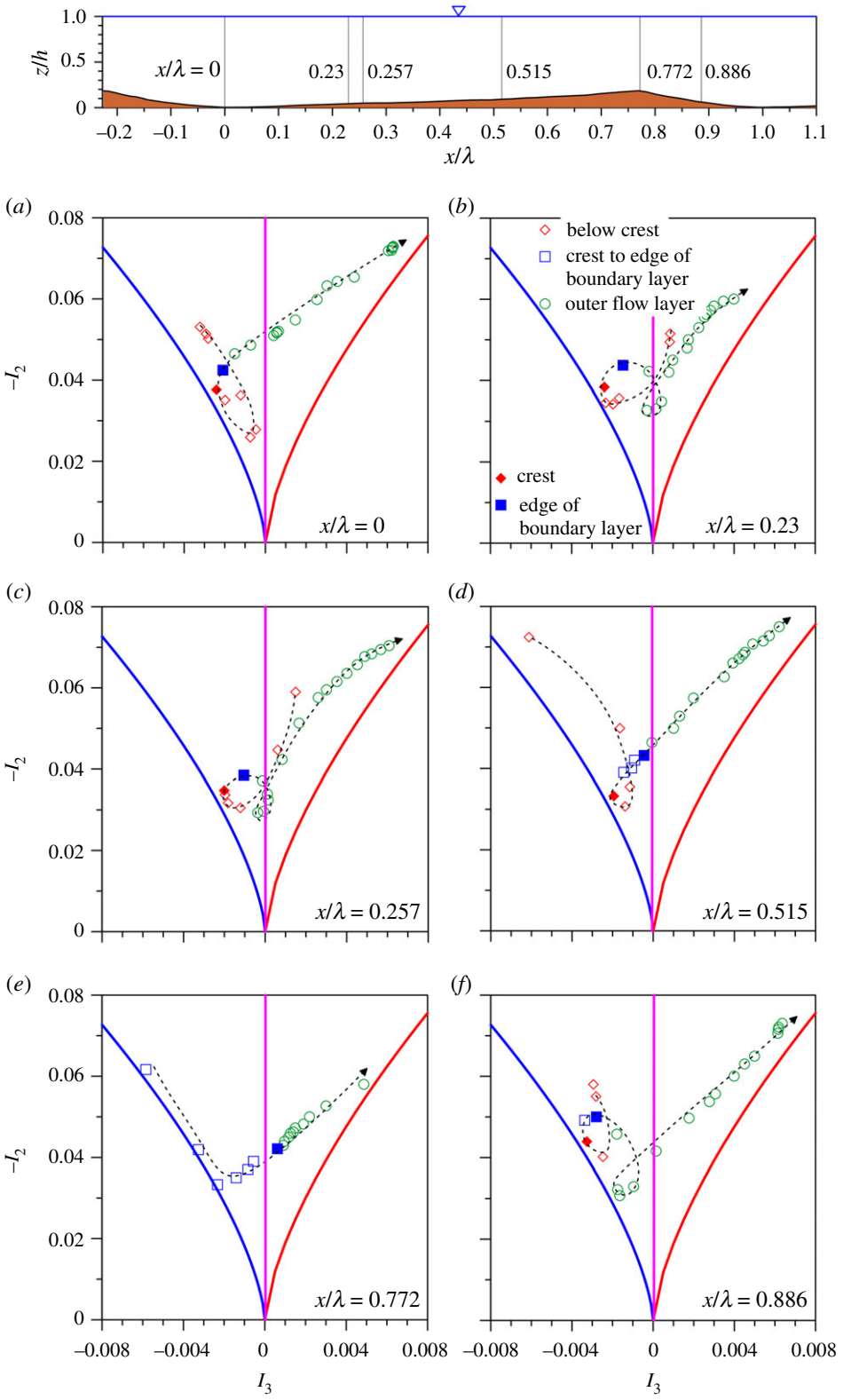

Figure 6. AIMs at (*a*) $x/\lambda = 0$ (trough), (*b*) 0.23 (reattachment point), (*c*) 0.257 (one-third of stoss-side), (*d*) 0.515 (two-thirds of stoss-side), (*e*) 0.772 (crest) and (*f*) 0.886 (mid of leeside). At the top, the sketch shows the horizontal locations of the vertical sections. (Online version in colour.)

looping pattern with an increase in vertical distance owing to the return to and departure from the quasi-three-dimensional isotropic state.

Figure 6*a–f* also shows that as the streamwise distance increases, the pattern of turbulence anisotropy strikingly changes. At the reattachment point and the one-third of the stoss-side (figure 6*b*,*c*), the data plots in the immediate near-bed flow zone stay close to the plane-strain limit. However, with an increase in vertical distance below the crest, the data plots have an affinity towards the axisymmetric contraction limit, forming a looping pattern within the crest to the edge of the boundary layer. As the vertical distance increases further, the data plots within the outer flow layer form another loop on the plane-strain limit line and afterwards gradually shift towards the axisymmetric expansion limit. At two-thirds of the stoss-side (figure 6*d*), the data plots in the near-bed flow zone emerge closely from the axisymmetric contraction limit and then follow a similar pattern as observed at the dune trough ($x/\lambda = 0$). Note that the appearance of the looping pattern on the plane-strain limit line at $x/\lambda = 0.23$ and $x/\lambda = 0.257$ gradually disappears with an increase in x/λ (figure 6*d*). At the top of the crest (figure 6*e*), the data plots reveal that the turbulence anisotropy appears to follow the axisymmetric contraction limit within the crest to the edge of the boundary layer. However, as the vertical distance increases, the data plots gradually take an anti-clockwise turn, crossing the plane-strain limit and then traversing towards the axisymmetric expansion limit. At the mid of the leeside (figure 6*f*), the data plots depict two successive looping patterns located approximately at the midway between the axisymmetric contraction and the plane-strain limits. However, within the outer flow layer, they gradually approach the axisymmetric expansion limit with an increase in vertical distance. Figure 6 also reveals that for all x/λ except $x/\lambda = 0.772$ (crest), the data points at the top of the crest (filled diamond symbols) always stay close to the left-curved side of the Lumley triangle, indicating the turbulence anisotropy to closely follow the axisymmetric contraction limit. On the other hand, the data points at the edge of the boundary layer (filled square symbols) suggests that the turbulence anisotropy appears to shift towards the plane-strain limit with an increase in x/λ up to $x/\lambda = 0.515$, crossing the plane-strain limit at $x/\lambda = 0.772$ and thereafter switching to the axisymmetric contraction limit.

It is worth noting that figure 6*a–f* does not provide an explicit representation of how the turbulence anisotropy at a given streamwise distance varies with the vertical distance. To this end, we introduce the anisotropic invariant function **F**. It is expressed as

$$\mathbf{F} = 1 + 9I_2 + 27I_3. \tag{4.8}$$

The anisotropic invariant function **F** offers an insight into the turbulence anisotropy ranging from the two-component limit (i.e. top-linear side of the Lumley triangle), corresponding to $\mathbf{F} = 0$ to the isotropic limit (i.e. bottom vertex of the Lumley triangle) corresponding to $\mathbf{F} = 1$. Therefore, it turns out that $0 \leq \mathbf{F} \leq 1$.

Figure 7*a–f* presents the data plots for the anisotropic invariant function **F** versus non-dimensional vertical distance z/h at various non-dimensional streamwise distances, $x/\lambda = 0$ (trough), 0.23 (reattachment point), 0.257 (one-third of stoss-side), 0.515 (two-thirds of stoss-side), 0.772 (crest) and 0.886 (mid of leeside), respectively. It appears that at the dune trough (figure 7*a*), the turbulence anisotropy in the near-bed flow zone has a tendency to return to the isotropic limit with an increase in vertical distance, forming a cusp at the separation line. Thereafter, it gradually departs from the isotropic limit as the vertical distance increases further, particularly within the outer flow layer. At the reattachment point (figure 7*b*), the pattern of turbulence anisotropy remains quite similar up to the edge of the boundary layer. However, the data plots exhibit the formation of two cusps, encapsulating the turbulence anisotropy to return to the isotropic limit as the vertical distance increases above the edge of the boundary layer. Within the outer flow layer, the data plots suggest that the turbulence anisotropy has a departure from the isotropic limit with a further increase in vertical distance. At one-third of the stoss-side (figure 7*c*), the pattern does not change significantly over the entire flow depth. However, it is noticeable that the upper cusp formed within the outer flow layer at $x/\lambda = 0.23$ and 0.257 gradually disappears with an

increase in vertical distance (figure 7*d*). At two-thirds of the stoss-side (figure 7*d*), the turbulence anisotropy in the near-bed flow zone is affined towards the two-component limit, but returns to the isotropic limit as the vertical distance increases below the crest. At the top of the crest, the return to the isotropic limit over the flow depth appears to be extreme. With an increase in x/λ, especially at the top of the crest and the mid of the leeside (figure 7*e*,*f*), the turbulence anisotropy in the near-bed flow zone slowly departs from the two-component limit and the formation of two cusps is eventually recovered at the mid of the leeside (figure 7*f*).

In order to have a clear picture of how the anisotropic function **F** for a given vertical distance varies with the streamwise distance, all the experimental data of figure 7 are plotted on a single $\mathbf{F}(z/h)$ frame, as shown in figure 8. Below the crest, the **F** varies approximately from 0.17 to 0.75, while far beyond the crest, it follows an almost constant range of 0.5–0.6.

Figures 6–8 are not capable of providing a quantitative estimation of the exact shape of ellipsoid formed by the principal components of Reynolds stresses. From the geometry, the equation of ellipsoid formed by the principal components $(\sigma_1, \sigma_2, \sigma_3)$ in (x_1, x_2, x_3) is expressed as

$$\frac{x_1^2}{\sigma_1^2} + \frac{x_2^2}{\sigma_2^2} + \frac{x_3^2}{\sigma_3^2} = 1. \tag{4.9}$$

To set a connection between the shape of the Reynolds stress tensor $\overline{u_i' u_j'}$ and the invariants of the Reynolds stress anisotropy tensor b_{ij}, it is required to link the eigenvalues of $\overline{u_i' u_j'}$ with b_{ij}. To this end, equation (4.2) produces the following relationship:

$$\omega_i = \frac{\sigma_i}{2k} - \frac{1}{3}. \tag{4.10}$$

For a given I_2 and I_3, equation (4.4) can be readily solved to obtain the complete set of eigenvalues ω_i (i = 1–3). With regards to the characteristic shapes in terms of eigenvalues ω_i, an oblate spheroid displays two equal eigenvalues that are larger than the other eigenvalue ($\omega_1 = \omega_2 > \omega_3$), resulting in a spheroid squeezed in one direction. On the other hand, a prolate spheroid exhibits a contrasting effect with one eigenvalue to be larger than the other two equal eigenvalues ($\omega_1 > \omega_2 = \omega_3$ or $\omega_1 = -2\omega_2$), resulting in a spheroid stretched in one direction. In principle, the ω_1 and ω_2 obey a generic set of inequalities given by equation (4.6). On the $\omega_1\omega_2$ frame, equation (4.6) forms a triangle. Figure 9*a*–*f* shows the data plots for ω_1 versus ω_2 at various non-dimensional streamwise distances, x/λ = 0 (trough), 0.23 (reattachment point), 0.257 (one-third of stoss-side), 0.515 (two-thirds of stoss-side), 0.772 (crest) and 0.886 (mid of leeside), respectively. Note that in figure 9*a*–*f*, the triangle on the $\omega_1\omega_2$ frame has been mapped from the Lumley triangle on $-I_2I_3$ frame. Here, the right and left sides of the triangle refer to the axisymmetric contraction and expansion limits, respectively, whereas the top side of the triangle corresponds to the two-component limit. In addition, the vertical line signifies the plane-strain limit. For a given ω_i, the corresponding σ_i can be readily found from equation (4.10) and subsequently, the shape of the stress ellipsoid can be identified. It appears that at the dune trough (figure 9*a*), the axisymmetric contraction to the oblate spheroid reduces with an increase in vertical distance below the crest, attaining a minimal value near the plane-strain limit. Thereafter, the oblate spheroid axisymmetric turbulence becomes more tapered as the data plots display a looping pattern with an increase in vertical distance up to the top of the crest. However, beyond the crest, the axisymmetric contraction to the oblate spheroid appears to reduce with an increase in vertical distance. Subsequently, the data plots cross the plane-strain limit, revealing that the axisymmetric expansion to the prolate spheroid within the outer flow layer increases as the vertical distance increases. At the reattachment point and one-third of the stoss-side (figure 9*b*,*c*), the oblate spheroid axisymmetric turbulence below the crest is more contracted with an increase in vertical distance. The data plots beyond the crest eventually approach the plane-strain limit, forming a looping pattern on the plane-strain limit and thereafter the axisymmetric expansion to the prolate spheroid increases, as the vertical distance increases within the outer flow layer. The looping pattern on the plane-strain limit vanishes at

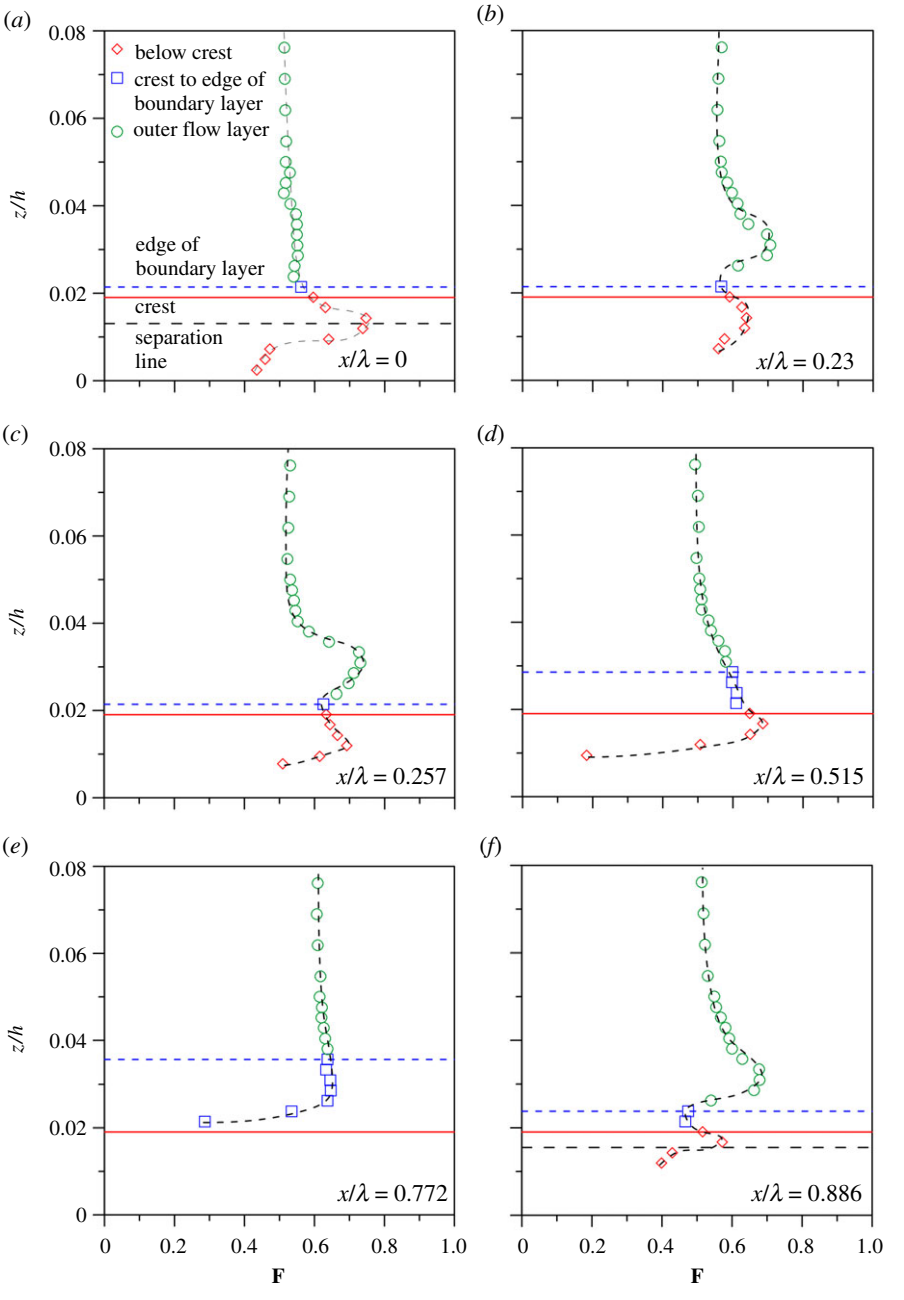

Figure 7. Anisotropic invariant function **F** versus non-dimensional vertical distance z/h at (*a*) $x/\lambda = 0$ (trough), (*b*) 0.23 (reattachment point), (*c*) 0.257 (one-third of stoss-side), (*d*) 0.515 (two-thirds of stoss-side), (*e*) 0.772 (crest) and (*f*) 0.886 (mid of leeside). (Online version in colour.)

two-thirds of the stoss-side (figure 9*d*). In the flow zone near the top of the crest (figure 9*e*), the stress ellipsoid appears to follow an oblate spheroid, because the data plots closely follow the axisymmetric contraction limit. However, in the outer flow layer, the axisymmetric expansion to the prolate spheroid tends to increase with an increase in vertical distance. At the mid of the leeside (figure 9*f*), some of the data plots immediately above the crest to the edge of the boundary layer reveal that the oblate spheroid axisymmetric turbulence tends to be more contracted

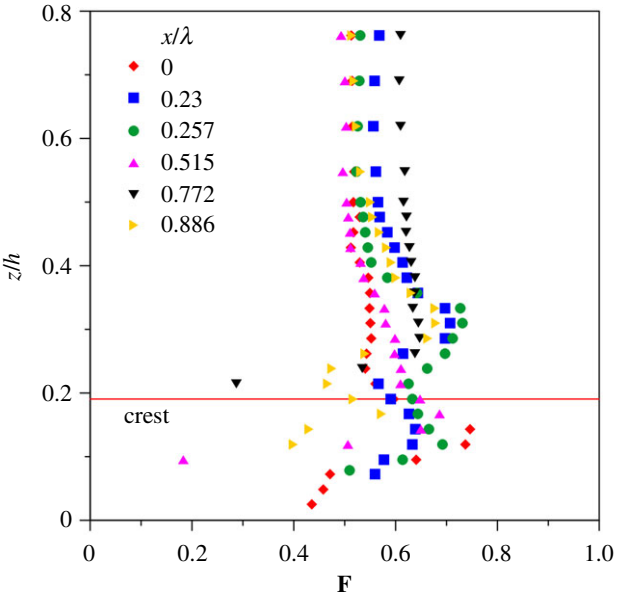

Figure 8. Anisotropic invariant function **F** versus non-dimensional vertical distance z/h at different values of x/λ. (Online version in colour.)

with an increase in vertical distance. However, as the vertical distance increases further, the prolate spheroid axisymmetric turbulence appears to be more contracted within the outer flow layer.

It is also interesting to examine how the shape of the stress ellipsoid for a given streamwise distance varies with the vertical distance. Figure 10*a–f* shows the data plots for the ω_2/ω_1 ratio versus non-dimensional vertical distance z/h at various non-dimensional streamwise distances, x/λ = 0 (trough), 0.23 (reattachment point), 0.257 (one-third of stoss-side), 0.515 (two-thirds of stoss-side), 0.772 (crest) and 0.886 (mid of leeside), respectively. The vertical lines ω_2/ω_1 = –0.5, 0 and 1 that refer to the axisymmetric expansion, plane-strain and axisymmetric contraction limits, respectively, are also marked. In the insets of figure 10*a–f*, the data plots for eccentricities, σ_2/σ_1 and σ_3/σ_2 versus z/h are illustrated in order to quantitatively picturize how the stress ellipsoid evolves with the vertical distance. Note that $\omega_2/\omega_1 = 1$ and $\sigma_3/\sigma_2 = 1$ correspond to oblate and prolate spheroids, respectively. At the dune trough (figure 10*a*), the shape of the stress ellipsoid appears to depart gradually from the oblate spheroid with an increase in vertical distance below the top of the crest, achieving a minimal value at the separation line. The stress ellipsoid is affined to the oblate spheroid at the top of the crest. However, the stress ellipsoid tends to become a prolate spheroid as the vertical distance increases within the outer flow layer. The data plots for σ_2/σ_1 and σ_3/σ_2 versus z/h suggest a similar conclusion (see the inset of figure 10*a*). It is worth noting that at $z/h \approx 0.45$, the data plots for σ_2/σ_1 and σ_3/σ_2 intersect each other, revealing that the sides of the stress ellipsoid follow a geometric progression ($\sigma_2^2 = \sigma_1\sigma_3$). The point of intersection of σ_2/σ_1 and σ_3/σ_2 data plots remains almost the same at one-third, two-thirds of the stoss-side and mid of the leeside (figure 10*c*,*d*,*f*). However, at the reattachment point (figure 10*b*) and at the top of the crest (figure 10*e*), the data plots for σ_2/σ_1 and σ_3/σ_2 appear to intersect at $z/h \approx 0.65$. Moreover, figure 10*a–f* indicates that the maximum contraction to the oblate spheroid occurs close to the top of the crest, whereas the maximum expansion to the prolate spheroid is prevalent within the outer flow layer, particularly near the free surface.

Indeed, understanding of the Reynolds stress anisotropy is the utmost imperative and subtle issue in reviewing the turbulence models based on the turbulence closure relationships, because it is involved in ascertaining the sensitivity of the turbulence quantities associated with the

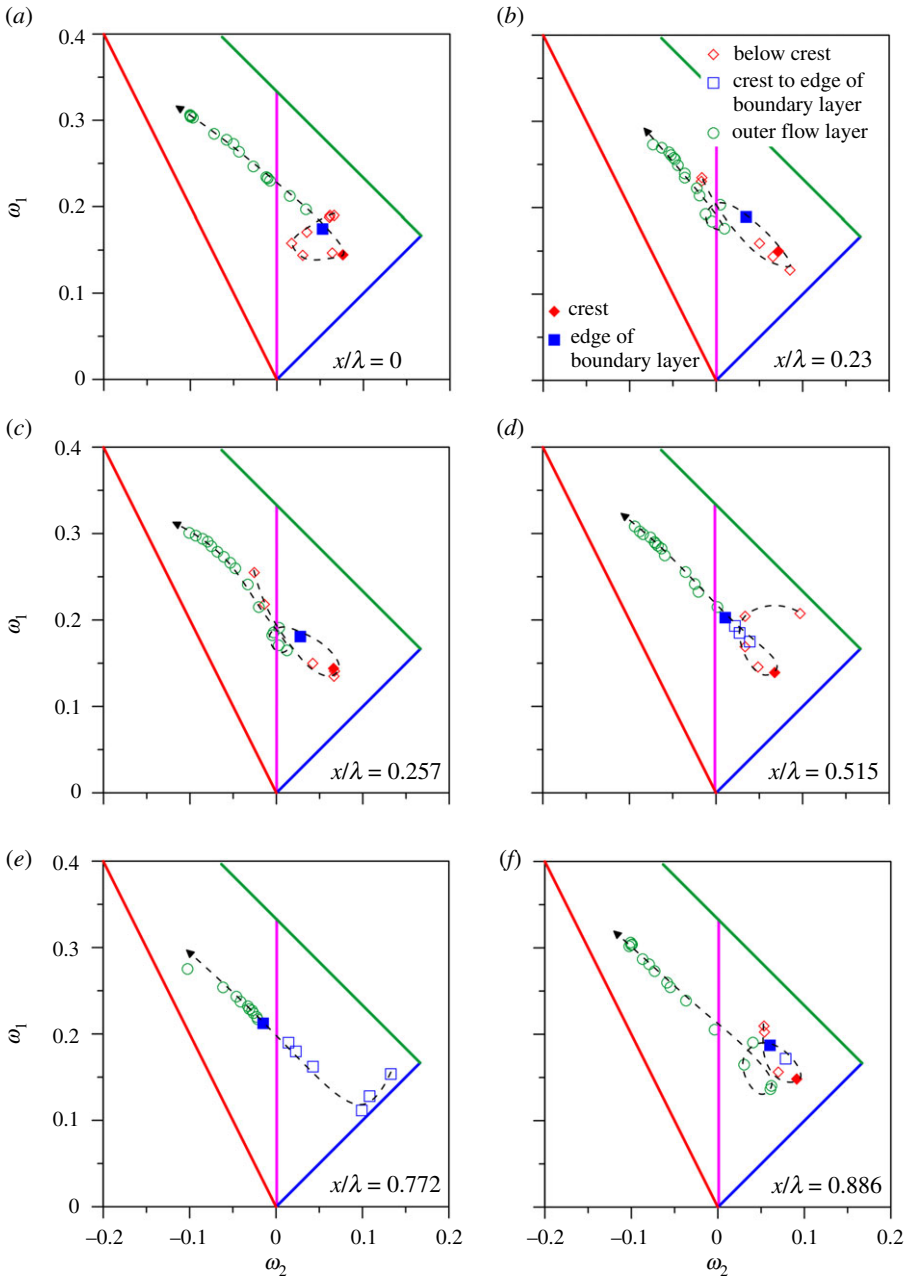

Figure 9. Eigenvalues ω_1 versus ω_2 at (*a*) $x/\lambda = 0$ (trough), (*b*) 0.23 (reattachment point), (*c*) 0.257 (one-third of stoss-side), (*d*) 0.515 (two-thirds of stoss-side), (*e*) 0.772 (crest) and (*f*) 0.886 (mid of leeside). (Online version in colour.)

turbulence models [48]. The significance of this study lies in its effectiveness in evaluating the turbulent topology at various streamwise sections over subaqueous dunes. The transformation of the three-dimensional flow structure to a two-dimensional frame formed by a new set of invariants, originally proposed by Rotta [43], is beneficial for developing predictive turbulence models and acts as the basis of the return to isotropy models [42,43]. The experimental data of this study would be helpful to enhance the performance of the current sophisticated numerical models for subaqueous dunes. In most cases, a parallel experimental campaign is required to check the legitimacy of numerical models for a wide range of flows. An urgent need for promising

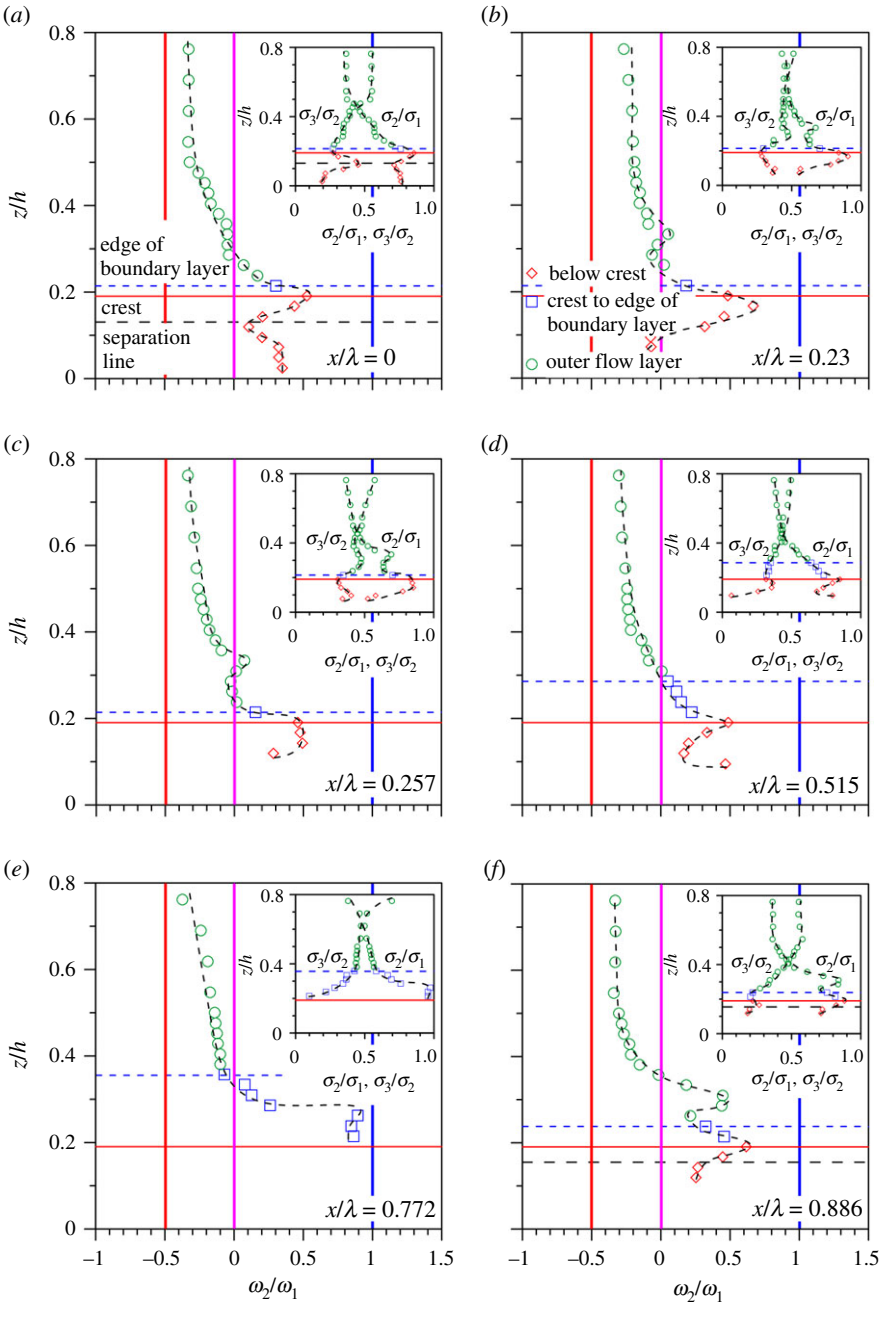

Figure 10. ω_2/ω_1 ratio versus non-dimensional vertical distance z/h at (*a*) $x/\lambda = 0$ (trough), (*b*) 0.23 (reattachment point), (*c*) 0.257 (one-third of stoss-side), (*d*) 0.515 (two-thirds of stoss-side), (*e*) 0.772 (crest) and (*f*) 0.886 (mid of leeside). (Online version in colour.)

numerical models can follow two different directions [69]. The first direction is to search for higher levels of closure in order to capture various turbulence phenomena, e.g. a Reynolds-stress level can be preferred to overcome the incapability of turbulent viscosity models in addressing the anisotropic decaying turbulence. In the same line, a structure-based level can be adopted to overcome the inability of Reynolds-stress models in estimating the rapid distortions having mean rotation. The second direction is to search for specific models within each class being more precise

than the existing models. Most often, a specific class of models is introduced by a set of governing equations that contain free constants and free coefficients, e.g. the class of k–ϵ turbulence models [69] and the algebraic Reynolds stress models [70–73]. The present experimental data can at least provide a guideline to improve the efficacy of numerical models, indicating a need for the so-called optimal model. For example, with regard to each model within the class, the error can be obtained as the weighted difference among the model estimation and the experimental observation. The optimal model therefore corresponds to the description of the free constants and free coefficients for which the error can be minimized. It is worth noting that in developing numerical models, accurate closure models backed up by experimental observations are sorely required. From the perspective of the realizability of turbulence models [74], an unrealizable closure model must be considered unacceptable, because it violates the realizability of Reynolds stress.

In the LES models for subaqueous dunes [26,32,33,38], the subgrid stresses were modelled by means of the eddy viscosity assumption [75]. The eddy viscosity ν_t takes the form of $\nu_t = (C_s\Delta)^2|\langle S_{ij}\rangle|$, where Δ is the subgrid characteristic length scale, $|\langle S_{ij}\rangle|$ is the magnitude of the local strain-rate tensor [$= (2\langle S_{ij}\rangle\langle S_{ji}\rangle)^{0.5}$] and $\langle\cdot\rangle$ represents a suitably chosen low-pass filter. The constant C_s was reported to be estimated from the Kolmogorov constant [76]. However, in the presence of mean shear, C_s does not remain a constant [75]. In the LES model of Omidyeganeh & Piomelli [32,33], the C_s was estimated using the dynamic model [75] together with the Lagrangian averaging technique [77]. However, a major difficulty of the LES models is the performance of the eddy-viscosity in the near-bed flow zone. For instance, the Smagorinsky model predicts a finite value of ν_t as long as the velocity gradient exists [78]. However, in the near-bed flow zone, the velocity fluctuations are excessively dampened, making the ν_t vanish. It therefore requires adopting a smaller value of C_s in order to maintain a turbulent flow in the physical system [78]. In the recent LES model for three-dimensional dunes [38], a refined choice of the ν_t was considered using a new subgrid scale model [78]. Therefore, an accurate estimation of C_s in flow over a complex geometry remains a challenging task unless new experimental measurements are available. The experimental data of this study can certainly shed new light on this aspect.

5. Conclusion

This paper features the turbulence anisotropy in flow over two-dimensional rigid dunes. At the dune trough and the top of the crest, the turbulence anisotropy in the near-bed flow zone closely follows the axisymmetric contraction limit. However, it switches from axisymmetric contraction to axisymmetric expansion limits with an increase in vertical distance within the outer flow layer. At various streamwise distances, the turbulence anisotropy up to the edge of the boundary layer forms a looping pattern as the vertical distance increases owing to the return to and departure from the quasi-three-dimensional isotropic state. The turbulence anisotropy in the immediate near-bed flow zone at the reattachment point and one-third of the stoss-side follows the plane-strain limit, whereas that at two-thirds of the stoss-side originates from the axisymmetric contraction limit. At all streamwise distances, the turbulence anisotropy close to the top of the crest follows the axisymmetric contraction limit. However, the turbulence anisotropy at the edge of the boundary layer tends to shift towards the plane-strain limit as the streamwise distance increases up to two-thirds of the stoss-side, crossing the plane-strain limit at the top of the crest and subsequently, moving towards the axisymmetric contraction limit. At a certain vertical distance within the outer flow layer, the sides of the stress ellipsoid appear to obey a geometric sequence. The maximum contraction to the oblate spheroid takes place near the top of the crest, while the maximum expansion to the prolate spheroid prevails near the free surface.

This study significantly advances the understanding of turbulence anisotropy in flow over two-dimensional rigid dunes, providing quantitative measures of the evolution of stress ellipsoid formed by the Reynolds stresses. The experimental data of this study provide a lucid picture of the components of the Reynolds stress tensor and clearly indicate their implications towards dune morphodynamics, where the sediment transport triggered by the near-bed stress field governs the

bed stability. In addition, this study not only offers a benchmark to calibrate the sophisticated numerical models, but also calls for a revision of the traditional turbulence models that are grounded on the isotropic hypothesis. Note that most of the existing turbulence models depend on the shear flow or the strain rate, indicating their inefficacy in capturing the flow with a high shear but low turbulence intensity. By contrast, this study makes use of the scaled Reynolds stress tensor, which does not need to be further scaled by the shear velocity, as traditionally done to represent the turbulence quantities in non-dimensional form. It turns out that the Reynolds stress anisotropy tensor can be deemed to be a representative quantity on which the numerical models should rely.

Data accessibility. The experimental data of this study can be accessed via this link: https://docs.google.com/spreadsheets/d/1pAHFpX5f6L1kc-SVw918WymEaTt5Z7W5penGMuK7qDs/edit?usp=sharing.

Authors' contributions. The conceptualization of the problem including the theoretical foundation was conceived by S.D and S.Z.A. The experiment was conducted by P.P. The experimental data were processed and analysed by P.P and E.P. The numerical code, figures and graphics were prepared by S.Z.A and E.P. The interpretation of the results and the preparation of the manuscript were done by S.D and S.Z.A. The research was supervised and directed by S.D.

Competing interests. We declare we have no competing interests.

Funding. No funding has been received for this article.

Acknowledgements. S.D. acknowledges the JC Bose Fellowship Award (JBD) for pursuing this work.

References

1. Dey S, Ali SZ. 2020 Fluvial instabilities. *Phys. Fluids* **32**, 061301 (doi:10.1063/5.0010038)
2. Seminara G. 2010 Fluvial sedimentary patterns. *Annu. Rev. Fluid Mech.* **42**, 43–66. (doi:10.1146/annurev-fluid-121108-145612)
3. Charru F, Andreotti B, Claudin P. 2013 Sand ripples and dunes. *Annu. Rev. Fluid Mech.* **45**, 469–493. (doi:10.1146/annurev-fluid-011212-140806)
4. Andreotti B, Claudin P, Douady S. 2002 Selection of dune shapes and velocities Part 1: dynamics of sand, wind and barchans. *Eur. Phys. J. B* **28**, 321–339. (doi:10.1140/epjb/e2002-00236-4)
5. Andreotti B, Claudin P, Douady S. 2002 Selection of dune shapes and velocities Part 2: a two-dimensional modelling. *Eur. Phys. J. B* **28**, 341–352. (doi:10.1140/epjb/e2002-00237-3)
6. Hersen P, Andersen KH, Elbelrhiti H, Andreotti B, Claudin P, Douady S. 2004 Corridors of barchan dunes: stability and size selection. *Phys. Rev. E* **69**, 011304 (doi:10.1103/PhysRevE.69.011304)
7. Andreotti B, Fourriére A, Ould-Kaddour F, Murray B, Claudin P. 2009 Giant aeolian dune size determined by the average depth of the atmospheric boundary layer. *Nature* **457**, 1120–1123. (doi:10.1038/nature07787)
8. Duran Vinent O, Andreotti B, Claudin P, Winter C. 2019 A unified model of ripples and dunes in water and planetary environments. *Nat. Geosci.* **12**, 345–350. (doi:10.1038/s41561-019-0336-4)
9. Kroy K, Sauermann G, Herrmann HJ. 2002 Minimal model for sand dunes. *Phys. Rev. Lett.* **88**, 054301 (doi:10.1103/PhysRevLett.88.054301)
10. Kroy K, Sauermann G, Herrmann HJ. 2002 Minimal model for aeolian sand dunes. *Phys. Rev. E* **66**, 031302 (doi:10.1103/PhysRevE.66.031302)
11. Dey S. 2014 *Fluvial hydrodynamics: hydrodynamic and sediment transport phenomena*. Berlin, Germany: Springer.
12. Cisneros J *et al*. 2020 Dunes in the world's big rivers are characterized by low-angle lee-side slopes and a complex shape. *Nat. Geosci.* **13**, 156–162. (doi:10.1038/s41561-019-0511-7)
13. Kwoll E, Venditti JG, Bradley RW, Winter C. 2016 Flow structure and resistance over subaquaeous high- and low-angle dunes. *J. Geophys. Res. Earth Surf.* **121**, 545–564. (doi:10.1002/2015JF003637)
14. Kwoll E, Venditti JG, Bradley RW, Winter C. 2017 Observations of coherent flow structures over subaqueous high- and low- angle dunes. *J. Geophys. Res. Earth Surf.* **122**, 2244–2268. (doi:10.1002/2017JF004356)
15. Dey S, Paul P, Fang H, Padhi E. 2020 Hydrodynamics of flow over two-dimensional dunes. *Phys. Fluids* **32**, 025106 (doi:10.1063/1.5144552)

16. Gilbert GK. 1914 The transportation of debris by running water. USGS Professional Paper No 86, US Ecological Survey, Washington, DC.
17. Brooks NH. 1958 Mechanics of streams with movable beds of fine sand. *Trans. Am. Soc. Civ. Eng.* **123**, 526–549.
18. Lyn DA. 1993 Turbulence measurements in open-channel flows over artificial bed forms. *J. Hydraul. Eng.* **119**, 306–326. (doi:10.1061/(ASCE)0733-9429(1993)119:3(306))
19. McLean SR, Nelson JM, Wolfe SR. 1994 Turbulence structure over two-dimensional bed forms: implications for sediment transport. *J. Geophys. Res. Oceans* **99**, 12 729–12 747. (doi:10.1029/94JC00571)
20. Bennett SJ, Best JL. 1995 Mean flow and turbulence structure over fixed, two-dimensional dunes: implications for sediment transport and bedform stability. *Sedimentology* **42**, 491–513. (doi:10.1111/j.1365-3091.1995.tb00386.x)
21. Kadota A, Nezu I. 1999 Three-dimensional structure of space-time correlation on coherent vortices generated behind dune crest. *J. Hydraul. Res.* **37**, 59–80. (doi:10.1080/00221689909498532)
22. Maddux TB, Nelson JM, McLean SR. 2003 Turbulent flow over three-dimensional dunes: 1. Free surface and flow response. *J. Geophys. Res. Earth Surface* **108**, 6009 (doi:10.1029/2003JF000017)
23. Venditti JG. 2007 Turbulent flow and drag over fixed two- and three-dimensional dunes. *J. Geophys. Res. Earth Surface* **112**, F04008 (doi:10.1029/2006JF000650)
24. McLean SR, Smith JD. 1986 A model for flow over two-dimensional bed forms. *J. Hydraul. Eng.* **112**, 300–317. (doi:10.1061/(ASCE)0733-9429(1986)112:4(300))
25. Nelson JM, Smith JD. 1989 Mechanics of flow over ripples and dunes. *J. Geophys Res. Oceans* **94**, 8146–8162. (doi:10.1029/JC094iC06p08146)
26. Stoesser T, Braun C, García-Villalba M, Rodi W. 2008 Turbulence structures in flow over two-dimensional dunes. *J. Hydraul. Eng.* **134**, 42–55. (doi:10.1061/(ASCE)0733-9429(2008)134:1(42))
27. McLean SR, Wolfe SR, Nelson JM. 1999 Spatially averaged flow over a wavy boundary revisited. *J. Geophys. Res. Oceans* **104**, 15743–15753. (doi:10.1029/1999JC900116)
28. McLean SR, Nikora VI, Coleman SE. 2008 Double-averaged velocity profiles over fixed dune shapes. *Acta Geophys.* **56**, 669–697. (doi:10.2478/s11600-008-0031-0)
29. Maddux TB, McLean SR, Nelson JM. 2003 Turbulent flow over three-dimensional dunes: 2. Fluid and bed stresses. *J. Geophys. Res. Earth Surface* **108**, 6010 (doi:10.1029/2003JF000018)
30. McLean SR, Nikora VI. 2006 Characteristics of turbulent unidirectional flow over rough beds: double-averaging perspective with particular focus on sand dunes and gravel beds. *Water Resour. Res.* **42**, W10409 (doi:10.1029/2005WR004708)
31. Coleman SE, Nikora VI. 2011 Fluvial dunes: initiation, characterization, flow structure. *Earth Surf. Proc. Landf.* **36**, 39–57. (doi:10.1002/esp.2096)
32. Omidyeganeh M, Piomelli U. 2013 Large-eddy simulation of three-dimensional dunes in a steady, unidirectional flow. Part 1. Turbulence statistics. *J. Fluid Mech.* **721**, 454–483. (doi:10.1017/jfm.2013.36)
33. Omidyeganeh M, Piomelli U. 2013 Large-eddy simulation of three-dimensional dunes in a steady, unidirectional flow. Part 2. Flow structures. *J. Fluid Mech.* **734**, 509–534. (doi:10.1017/jfm.2013.499)
34. Omidyeganeh M, Piomelli U, Christensen KT, Best JL. 2013 Large eddy simulation of interacting barchan dunes in a steady, unidirectional flow. *J. Geophys. Res. Earth Surface* **118**, 2089–2104. (doi:10.1002/jgrf.20149)
35. Chang K, Constantinescu G. 2013 Coherent structures in flow over two-dimensional dunes. *Water Resour. Res.* **49**, 2446–2460. (doi:10.1002/wrcr.20239, 2013)
36. Khosronejad A, Sotiropoulos F. 2014 Numerical simulation of sand waves in a turbulent open channel flow. *J. Fluid Mech.* **753**, 150–216. (doi:10.1017/jfm.2014.335)
37. Sotiropoulos F, Khosronejad A. 2016 Sand waves in environmental flows: insights gained by coupling large-eddy simulation with morphodynamics. *Phys. Fluids* **28**, 021301 (doi:10.1063/1.4939987)
38. Liu Y, Fang H, Huang L, He G. 2019 Numerical simulation of the production of three-dimensional sediment dunes. *Phys. Fluids* **31**, 096603 (doi:10.1063/1.5108741)
39. Ali N, Hamilton N, Calaf M, Cal RB. 2019 Classification of the Reynolds stress anisotropy tensor in very large thermally stratified wind farms using colormap image segmentation. *J. Renew. Sustain. Energy* **11**, 063305 (doi:10.1063/1.5113654)

40. Lumley JL, Newman GR. 1977 The return to isotropy of homogeneous turbulence. *J. Fluid Mech.* **82**, 161–178. (doi:10.1017/S0022112077000585)
41. Pope SB. 2000 *Turbulent flows*. Cambridge, UK: Cambridge University Press.
42. Choi K-S, Lumley JL. 2001 The return to isotropy of homogeneous turbulence. *J. Fluid Mech.* **436**, 59–84. (doi:10.1017/S002211200100386X)
43. Rotta JC. 1951 Statistische theorie nichthomogener turbulenz. *Z. Phys.* **129**, 547–572. (doi:10.1007/BF01330059)
44. Smyth WD, Moum JN. 2000 Anisotropy of turbulence in stably stratified mixing layers. *Phys. Fluids* **12**, 1343 (doi:10.1063/1.870386)
45. Schumann U, Patterson GS. 1978 Numerical study of the return of axisymmetric turbulence to isotropy. *J. Fluid Mech.* **88**, 711–735. (doi:10.1017/S0022112078002359)
46. Mestayer P. 1982 Local isotropy and anisotropy in a high-Reynolds-number turbulent boundary layer. *J. Fluid Mech.* **125**, 475–503. (doi:10.1017/S0022112082003450)
47. Smalley RJ, Leonardi S, Antonia RA, Djenidi L, Orlandi P. 2002 Reynolds stress anisotropy of turbulent rough wall layers. *Exp. Fluids* **33**, 31–37. (doi:10.1007/s00348-002-0466-z)
48. Keirsbulck L, Labraga L, Mazouz A, Tournier C. 2002 Influence of surface roughness on anisotropy in a turbulent boundary layer flow. *Exp. Fluids* **33**, 497–499. (doi:10.1007/s00348-002-0424-9)
49. Leonardi S, Orlandi P, Djenidi L, Antonia RA. 2004 Structure of turbulent channel flow with square bars on one wall. *Int. J. Heat Fluid Flow* **25**, 384–392. (doi:10.1016/j.ijheatfluidflow.2004.02.022)
50. Sarkar S, Dey S. 2015 Turbulent length scales and Reynolds stress anisotropy downstream of a wall mounted sphere. *J. Hydraul. Res.* **53**, 649–658. (doi:10.1080/00221686.2015.1086830)
51. Dey S, Swargiary D, Sarkar S, Fang H, Gaudio R. 2018 Turbulence features in a wall-wake flow downstream of a wall-mounted vertical cylinder. *Eur. J. Mech. B Fluids* **69**, 46–61. (doi:10.1016/j.euromechflu.2018.01.003)
52. Sarkar S, Ali SZ, Dey S. 2019 Turbulence in wall-wake flow downstream of an isolated dunal bedform. *Water* **11**, 1975 (doi:10.3390/w11101975)
53. Hamilton N, Cal RB. 2015 Anisotropy of the Reynolds stress tensor in the wakes of wind turbine arrays in Cartesian arrangements with counter-rotating rotors. *Phys. Fluids* **27**, 015102 (doi:10.1063/1.4903968)
54. Hamilton N, Tutkun M, Cal RB. 2017 Anisotropic character of low-order turbulent flow descriptions through the proper orthogonal decomposition. *Phys. Rev. Fluids* **2**, 014601 (doi:10.1103/PhysRevFluids.2.014601)
55. Ali N, Hamilton N, Cortina G, Calaf M, Cal RB. 2018 Anisotropy stress invariants of thermally stratified wind turbine array boundary layers using large eddy simulations. *J. Renew. Sustain. Energy* **10**, 013301 (doi:10.1063/1.5016977)
56. Camp EH, Cal RB. 2019 Low-dimensional representations and anisotropy of model rotor versus porous disk wind turbine arrays. *Phys. Rev. Fluids* **4**, 024610 (doi:10.1103/PhysRevFluids.4.024610)
57. Pouransari Z, Biferale L, Johansson AV. 2015 Statistical analysis of the velocity and scalar fields in reacting turbulent wall-jets. *Phys. Fluids* **27**, 025102 (doi:10.1063/1.4906370)
58. Dey S, Ravi Kishore G, Castro-Orgaz O, Ali SZ. 2019 Turbulent length scales and anisotropy in submerged turbulent plane offset jets. *J. Hydraul. Eng.* **145**, 04018085 (doi:10.1061/(ASCE)HY.1943-7900.0001559)
59. Bradley RW, Venditti JG. 2017 Reevaluating dune scaling relations. *Earth-Sci. Rev.* **165**, 356–376. (doi:10.1016/j.earscirev.2016.11.004)
60. Chow VT. 1959 *Open channel hydraulics*. New York, NY: McGraw-Hill.
61. Dey S, Ali SZ. 2019 Bed sediment entrainment by streamflow: state of the science. *Sedimentology* **66**, 1449–1485. (doi:10.1111/sed.12566)
62. Ali SZ, Dey S. 2016 Hydrodynamics of sediment threshold. *Phys. Fluids* **28**, 075103 (doi:10.1063/1.4955103)
63. Dey S, Ali SZ. 2017 Stochastic mechanics of loose boundary particle transport in turbulent flow. *Phys. Fluids* **29**, 055103 (doi:10.1063/1.4984042)
64. Dey S, Ali SZ. 2018 Review article: advances in modeling of bed particle entrainment sheared by turbulent flow. *Phys. Fluids* **30**, 061301 (doi:10.1063/1.5030458)
65. Sumer BM, Chua LHC, Cheng N-S, Fredsœ J. 2003 Influence of turbulence on bed load sediment transport. *J. Hydraul. Eng.* **129**, 585–596. (doi:10.1061/(ASCE)0733-9429(2003)129:8(585))

66. Banerjee S, Krahl R, Durst F, Zenger CH. 2007 Presentation of anisotropy properties of turbulence, invariants versus eigenvalue approaches. *J. Turbul.* **8**, 1–27. (doi:10.1080/14685240701506896)
67. Reynolds WC, Kassinos SC. 1995 One-point modelling of rapidly deformed homogeneous turbulence. *Proc. R. Soc. Lond. A* **451**, 87–104. (doi:10.1098/rspa.1995.0118)
68. Simonsen AJ, Krogstad PÅ. 2005 Turbulent stress invariant analysis: clarification of existing terminology. *Phys. Fluids* **17**, 088103 (doi:10.1063/1.2009008)
69. Pope SB. 1999 A perspective on turbulence modeling. In *Modeling complex turbulent flows* (eds MD Salas, JN Hefner, L Sakell), pp. 53–67, ICASE/LaRC Interdisciplinary Series in Science and Engineering, vol 7, Dordrecht, The Netherlands: Springer.
70. Taulbee DB. 1992 An improved algebraic Reynolds stress model and corresponding nonlinear stress model. *Phys. Fluids A: Fluid Dyn.* **4**, 2555 (doi:10.1063/1.858442)
71. Girimaji SS. 1996 Fully explicit and self-consistent algebraic Reynolds stress model. *Theoret. Comput. Fluid Dyn.* **8**, 387–402. (doi:10.1007/BF00455991)
72. Girimaji SS. 1999 Development of algebraic Reynolds stress model for non-equilibrium turbulence. In *Modeling complex turbulent flows* (eds MD Salas, JN Hefner, L Sakell), pp. 139–160, ICASE/LaRC Interdisciplinary Series in Science and Engineering, vol 7, Dordrecht, The Netherlands: Springer.
73. Wallin S, Johansson AV. 2000 An explicit algebraic Reynolds stress model for incompressible and compressible turbulent flows. *J. Fluid Mech.* **403**, 89–132. (doi:10.1017/S0022112099007004)
74. Girimaji SS. 2004 A new perspective on realizability of turbulence models. *J. Fluid Mech.* **512**, 191–210. (doi:10.1017/S0022112004009656)
75. Germano M, Piomelli U, Moin P, Cabot WH. 1991 A dynamic subgrid-scale eddy viscosity model. *Phys. Fluids A: Fluid Dyn.* **3**, 1760–1765. (doi:10.1063/1.857955)
76. Lilly DK. 1992 A proposed modification of the Germano subgrid-scale closure method. *Phys. Fluids A: Fluid Dyn.* **4**, 633–635. (doi:10.1063/1.858280)
77. Meneveau C, Lund TS, Cabot WH. 1996 A Lagrangian dynamic subgrid-scale model of turbulence. *J. Fluid Mech.* **319**, 353–385. (doi:10.1017/S0022112096007379)
78. Nicoud F, Ducros F. 1999 Subgrid-scale stress modelling based on the square of the velocity gradient tensor. *Flow Turbul. Combust.* **62**, 183–200. (doi:10.1023/A:1009995426001)